science.sciencemag.org/content/364/6439/485/suppl/DC1

Supplementary Materials for

Genetic diversity of tumors with mismatch repair deficiency influences anti–PD-1 immunotherapy response

Rajarsi Mandal,* Robert M. Samstein,* Ken-Wing Lee,* Jonathan J. Havel, Hao Wang, Chirag Krishna, Erich Y. Sabio, Vladimir Makarov, Fengshen Kuo, Pedro Blecua, Apoorva T. Ramaswamy, Jennifer N. Durham, Bjarne Bartlett, Xiaoxiao Ma, Raghvendra Srivastava, Sumit Middha, Ahmet Zehir, Jaclyn F. Hechtman, Luc GT Morris, Nils Weinhold, Nadeem Riaz, Dung T. Le, Luis A. Diaz Jr., Timothy A. Chan†

*These authors contributed equally to this work.
†Corresponding author. Email: chant@mskcc.org

Published 3 May 2019, *Science* **364**, 485 (2019)
DOI: 10.1126/science.aau0447

This PDF file includes:

Materials and Methods
Figs. S1 to S15
Captions for tables S1 and S2
Tables S3 to S6
References

Other Supplementary Materials for this manuscript include the following:
(available at science.sciencemag.org/content/364/6439/485/suppl/DC1)

Tables S1 and S2 (PDF)

Materials and Methods

MSH2-knock out in B16F10 and CT26 cells.

pSpCas9n(BB)-2A-GFP (PX461) was a gift from F. Zhang (Addgene plasmid #48140) (*21*). Guide RNA sequences (5'-CGGTGCGCCTCTTCGACCGC-3') and (5'-GCACGGAGAGGACGCGCTGC-3') targeting mouse *Msh2* exon 1 were cloned into PX461 plasmid and co-transfected into mouse melanoma B16F10 and CT26 mouse colon carcinoma cells using GenJet™ (SignaGen®) *In Vitro* DNA Transfection Reagent following the manufacturer's protocol. 48 hours following transfection, GFP^+ cells were seeded at one cell per 96-well by the Flow Cytometry Core Facility (FCCF) at Memorial Sloan Kettering Cancer Center. Cells were grown in RPMI supplemented with 10% FBS. Single cell clones were expanded and depletion of MSH2 was confirmed by immunoblotting (anti-MSH2 monoclonal antibody (FE11), Invitrogen Antibodies), and PCR cloning and sequencing of the edited genomic region (PCR cloning kit, NEB), with additional verification using high-throughput sequencing. Confirmed *Msh2*$^{-/-}$ single cell clones were expanded and used for serial passaging and downstream *in vivo* studies further described below. Single subclones were used in both cell lines across comparator arms in order to make sequencing and growth kinetic data directly comparable across arms within a single experiment.

Accumulation of microsatellite instability and mutations in B16F10/CT26 cells.

Control and *Msh2*-deficient B16F10/CT26 cell lines were serially passaged for continuous lengths of time under standard tissue culture conditions. The cellular doubling time was approximated to be roughly 15 hours, facilitating timely mutational generation in the polyploid tested lines. Cells from 1 month ("MSI-intermediate") and 4 months ("MSI-high") were frozen

under standard cell-specific freezing conditions with heat inactivated FBS + 10% DMSO cryoprotectant. Cells (pools of daughter cells derived from a single subclone) were collected at defined time points and underwent whole-exome sequencing (WES, 150x mean coverage; 650x, mean coverage for the B16F10 immunoediting analyses) at the Integrative Genomics Operation (IGO) at Memorial Sloan Kettering Cancer Center. WES reads were aligned to the mm19 reference mouse genome and mutations in coding genes were identified (against normal splenic DNA from their respective syngeneic hosts, C57BL/6 (B16F10), BALB/c (CT26)) by a genomics mutation pipeline using 4 independent mutational callers: MuTect 1.1.4, Strelka 2.7.1, SomaticSniper 1.0.4, and Varscan 2.3.7 (*22*, *23*). Tumor and variant coverage required at least 10 and 7 reads respectively to call a variant, and the variant could not be present in the germline. Tumor mutation load was determined as the number of non-synonymous mutations in the exome. Insertions and deletions were determined using Varscan and Strelka with default settings. Only indels called by both callers were included. SNVs with an allele read count of less than 4 or with corresponding normal coverage of less than 10 reads were filtered out (**Fig. S4)**. Neoantigen prediction calling was performed and based on MHC-binding prediction-(NetMHCpan 4.0, http://www.cbs.dtu.dk/services/NetMHCpan/). Sequencing files have been deposited into Sequence Read Archive (SRA) (https://www.ncbi.nlm.nih.gov/sra) and can be found under the following accession numbers: SAMN09941220, SAMN09941221, SAMN09941222, SAMN09941223, SAMN09941224, SAMN09941225, SAMN09941226, SAMN09941227, SAMN09941228, SAMN09941229, SAMN09941230, SAMN09941231, SAMN09941232, and SAMN09941233.

***In vivo* analysis of anti-PD-1 efficacy.**

All cells lines were tested and confirmed negative for mycoplasma infection prior to the murine experiments. Cells at both timepoints were thawed, expanded, and injected into separate mice simultaneously in the same experiment to prevent any batch effects. 1 x 10^5 B16F10 or 1.5 x 10^5 CT26 cells in 100 µl of PBS were injected into the left flanks of 6-week old female C57BL/6 (B16F10) or BALB/c (CT26) mice (Jackson Laboratories). Mice with clinically palpable tumors (2 mm in diameter) were randomized into isotype control IgG antibody or anti-mPD-1 treatment groups (~10 days post-injection). IgG or anti-mPD-1 antibodies (6 mg/kg) were administered intraperitoneally in 100 µl of PBS every 3-4 days. Tumor volumes were measured twice weekly and calculated by the formula: $\frac{(Length)\ x\ (Width)^2}{2}$. A separate experimental replicate was performed to ensure reproducibility of the tumor growth kinetic phenotype observed in MSI-high tumor lines. Additionally, a separate, independent single cell clone was selected in the CT26 line and was subjected to serially passaging, whole exome sequencing (150x), and tumor growth kinetic analysis on the MSI-intermediate and MSI-high cell lines and confirmed the same tumor growth therapeutic phenotype.

Multiplex immunofluorescence staining of tumor tissue.

Mice were euthanized by carbon dioxide and the flank tumors were resected at 24 days post-tumor injection. Tumors were fixed in 4% paraformaldehyde in PBS overnight at 4ºC, and then placed in 70% ethanol at 4ºC. Tissue was embedded in paraffin, sectioned, and stained by the Molecular Cytology Core Facility (MCCF) at Memorial Sloan Kettering Cancer Center. DAPI and antibodies against CD3, CD8, PD-1 were provided from MCCF at MSKCC and used according to previously

validated, standard concentrations. Slides were scanned by fluorescence Mirax Scanner through the MCCF at MSKCC.

Flow cytometry analysis.

Mice were euthanized by carbon dioxide and the flank tumors were resected at 24 days post-tumor injection. Fresh tumors were pooled by experimental arm and immediately dissociated into single cell suspensions using a gentle MACS tissue dissociator (Miltenyi Biotech). Cell suspensions were stained using murine CD3, CD4, CD8, CD45, and Live-Dead zombie aqua antibodies. Stained single cell suspensions were analyzed using the LSRII (BD) flow cytometric analyzer. Quantitative data analysis was performed using FCS Express 6 (De Novo Software).

Mouse Transcriptome and Genomic Analysis

For RNA-seq analysis, FASTQ files were aligned against the mm10 assembly by STAR. Gene level count values were then computed by the *summarizeOverlaps* function from the R package "Genomic Alignments" with mm10 *KnownGene* as the base gene model. The Union counting mode was used and only mapped paired reads were considered. Differential gene expression analysis was conducted using the R package "DESeq2". For pathway analysis, differentially expressed genes were used as input to the R package "ClusterProfiler". For genomic mutational analysis, mutational variants were called as detailed above. The tumor mutational allele frequency (MAF) was calculated for every SNV/Indel in a sample and represents the post-filtering fraction of reads carrying that mutation. Kernel density estimate plots of specified mutations were generated using the seaborn statistical data visualization platform for Python. Purity corrections were performed using ESTIMATE, a validated NGS-based RNA-sequencing

tool (*24*) to infer the relative amount of stromal and immune contamination in each sample. Sequencing data for MAF analyses represent a mean a coverage of 650x resolution. Threshold for MAF frequencies were set to greater than .04, to remove sequencing artifact of low variant calls, and to less than .75, to remove germline/drift mutations of from the reference C57BL/6 genome (corresponding to greater than 3 out of 4 alleles given the tetraploidy of the cells line).

Pan-Cancer TCGA MSI Analysis

The cytolytic activity of the immune infiltrate (CYT score) was defined based on the transcript levels of two key cytolytic effectors, namely GZMA (granzyme A) and PRF1 (perforin), which are upregulated upon CD8+ T cell activation (*25*). For this, RNASeqV2 data were obtained from the Broad's Institute Firehose (01/28/2016). Following [https://gdac.broadinstitute.org], we took, per tumor, the geometric mean of the expression in transcripts ('scaled estimate' values in the expression data, representing TPM as calculated by RSEM) in the two genes specified above (**Table S1**).

MSIsensor

The BAM (*.bam) files for each tumor of the TCGA cohort (1/28/2016) across 24 cancer types were downloaded from the Broad's Institute GDC Data Portal (https://portal.gdc.cancer.gov). MSI Sensor (*26*) was subsequently run for each one of the 24 cancer types with the authors' specified default values, within an SGE parallel environment (**Table S2**). A given tumor was deemed be MSI-HIGH if its corresponding score was greater than a threshold of 3.5, as specified in the original publication. This threshold was found to be independent of the tissue of origin, as previously reported (*27*). MSI-LOW and MSS tumors were not found to be phenotypically different by the authors of this manuscript, in accordance with previous reports (*27*, *28*)

Patient clinical sequencing analysis.

Genetic whole exome sequencing BAM (*.bam) files were analyzed from a published cohort of anti-PD-1 treated patients with MMR deficient and proficient tumors (*29*). Clinical data was retrieved from the original publication and updated with most recent clinical data since time of original publication (**Table S3**). MSIsensor score was calculated from the tumor/normal .bam files using the published available tool (version 0.2) (*26*). MSIsensor scores were compared between MMR proficient and deficient tumors as determined by clinical testing using the student's t-test.

For MSK-IMPACT clinical data, patient data was previously reported. The clinical endpoint used for analysis was overall survival, defined as the length of time from treatment start to time to event (survival or censor). Following institutional review board approval, institutional pharmacy records were used to identify patients who received at least one dose of immune checkpoint blockade and then cross-referenced with patients who had MSK-IMPACT testing done in the context of routine clinical care and were clinically designated MSI-H by conventional PCR or IHC criteria. Details of tissue processing and next generation sequencing and analysis have been previously described. For the analyses presented in this study, we obtained next-generation sequencing data and associated clinical data available on the cBioportal.

Statistical analysis

All groups represent data expressed as means ± SEM unless otherwise specified. Analyzed pooled samples represent absolute values. Tumor volumes were compared between two treatment groups at each time point using unpaired Student's *t*-tests with Holm Sidak correction

for testing at multiple timepoints. T cell infiltration and TAF distributions were analyzed as indicated using 1-way ANOVA with multiple testing correction using Dunnett's test for comparisons to a single control group or Tukey's test for pairwise comparisons as indicated in figure legends. Fisher's exact test was used for the comparison of two proportions (i.e. percent microsatellite unstable sites, SNV/indel proportions, SNV/indel editing) as specified in respective figure legends. The mean delta (from post to pre-therapy) MAFs between isotype control vs. anti-PD-1 treatment for each respective line was analyzed using one-way ANOVA with Holm Sidak correction for testing two cell lines as indicated in the figure legend. Unpaired two-tailed Mann Whitney U test was performed for the cytolytic score that has a skewed distribution, and unpaired t tests for MSI sensor score. Pearson's correlation was used to characterize the correlation between MSI sensor score with indels and SNVs. Kaplan Meier curves were used to visualize overall survival (OS) and log rank test was performed to compare the overall survival (OS) of MSI-High and MSI-intermediate patients. Cox regression analysis was conducted to assess the impact of high MSI sensor score on OS, and multivariable Cox model was used to evaluate its effect adjusting for the potential confounding factors of histology and TMB. Consideration for statistical significance was such that $p<.05$. All statistical tests were two-sided and performed using GraphPad Prism and R software using the *survival* package.

A.

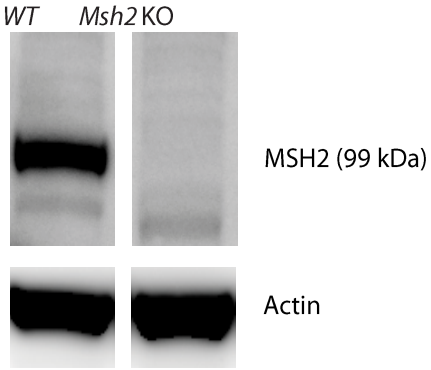

B.

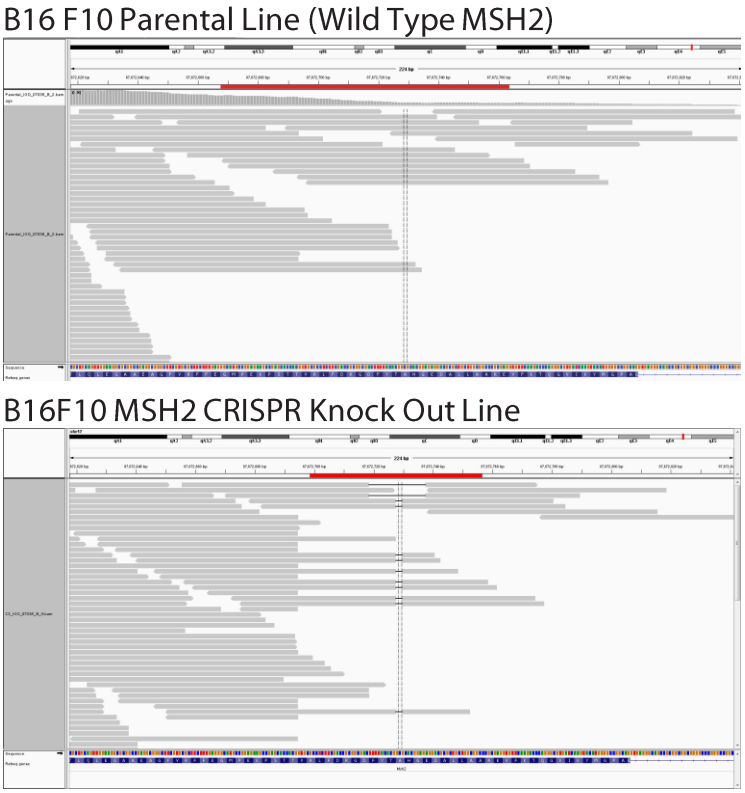

Fig. S1.

Validation of CRISPR-Cas9 *Msh2* gene knockout in B1610 mouse melanoma cell line. (a) Western immunoblot depicting actin control and wild type MSH2 protein (99kDa) and protein level knockout in the *Msh2* gene knockout cell line. (b) Integrated genomics viewer (IGV) plots depicting wild type *Msh2* in between the guide RNAs in the unedited wild type *Msh2* parental line and the *Msh2* CRISPR knockout line confirming bi-allelic gene knockout in the edited line.

A.

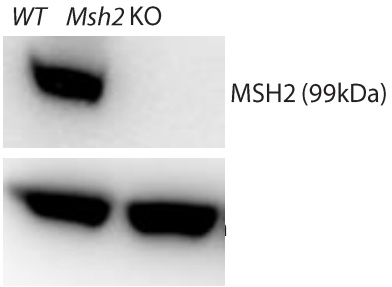

B.

CT26 Parental Line (Wild Type MSH2)

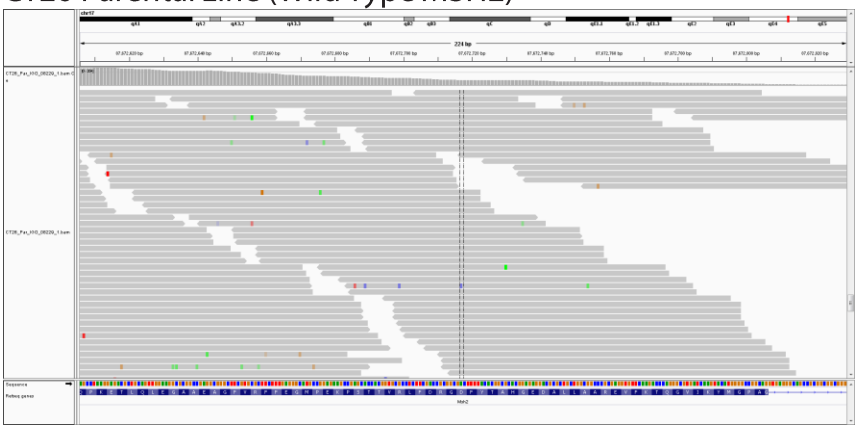

CT26 MSH2 CRISPR Knock Out Line

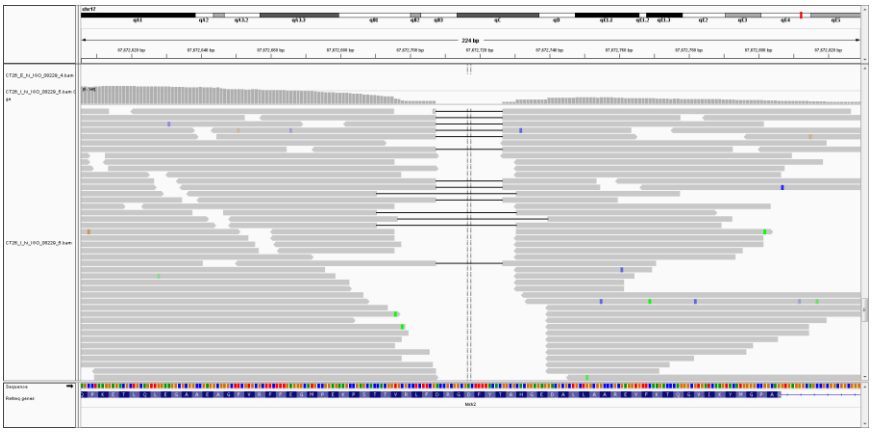

Fig. S2.

Validation of CRISPR-Cas9 *Msh2* gene knockout in CT26 colon carcinoma cell line. (a) Western immunoblot depicting actin control and wild type MSH2 protein (99kDa) and protein level knockout in the *Msh2* gene knockout cell line. (b) Integrated genomics viewer (IGV) plots depicting wild type *Msh2* in between the guide RNAs in the unedited wild type *Msh2* parental line and the *Msh2* CRISPR knockout line confirming bi-allelic gene knockout in the edited line.

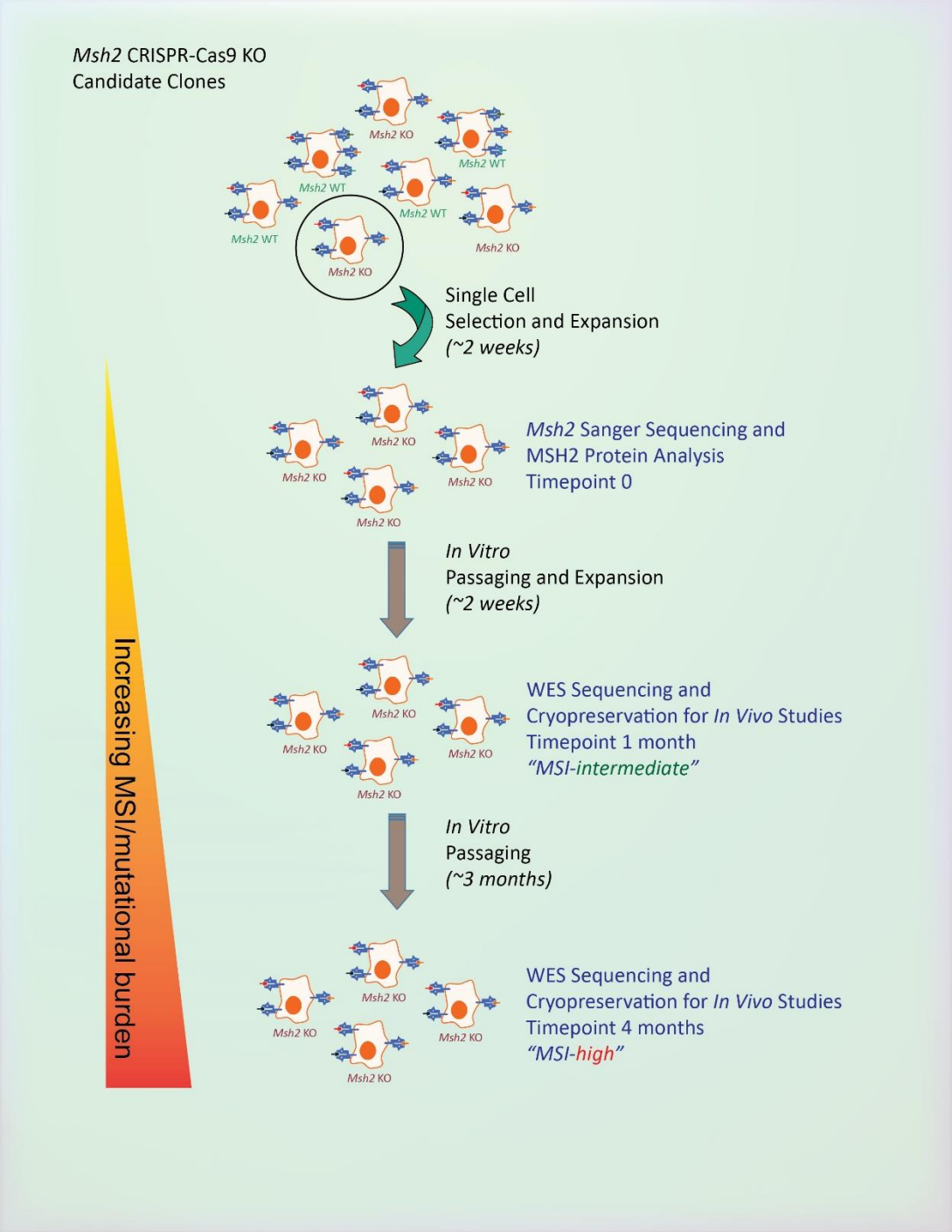

Fig. S3.

Mutational evolution following anti-PD-1-therapy in MSI-H tumor cells. In vitro mutational generation in MMR-deficient tumor cells. Illustrative schematic depicting subcloning strategy and *in vitro* mutational generation after serial passaging in MMR-deficient tumors cells.

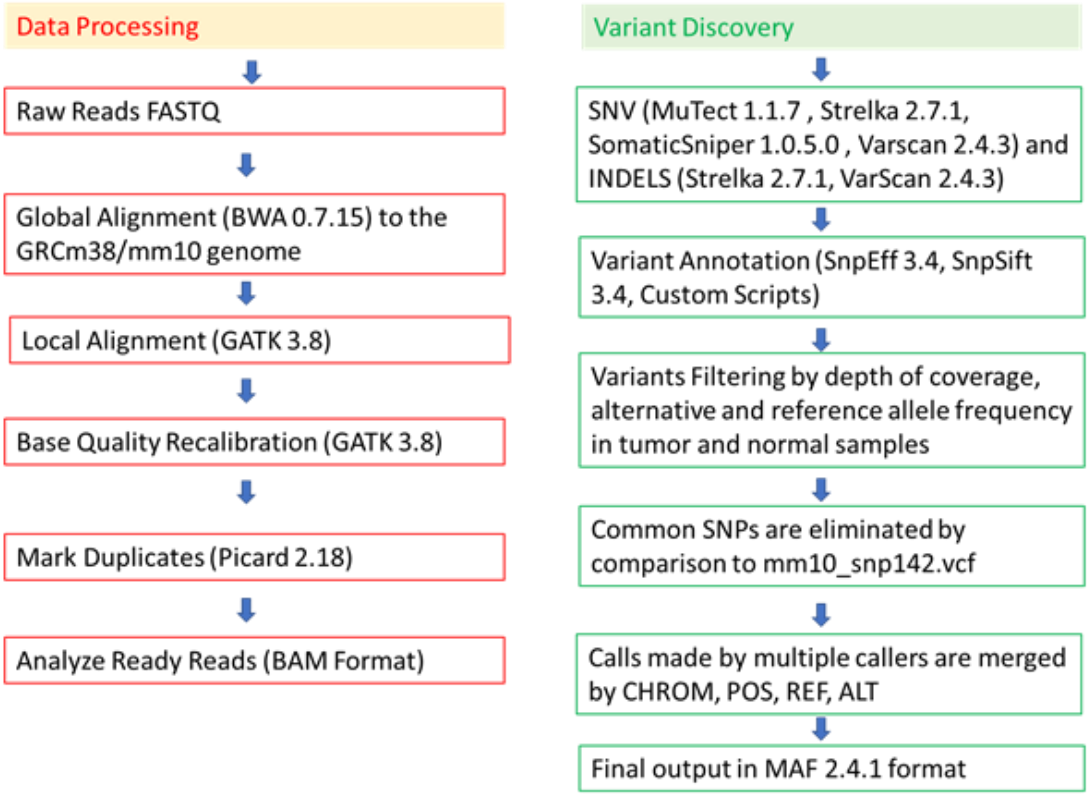

Fig. S4.

Data processing and variant discovery. Graphical illustration of approach utilized for data processing and variant discovery applied to whole exome sequencing data to determine mutational burden from exonic coding sequences.

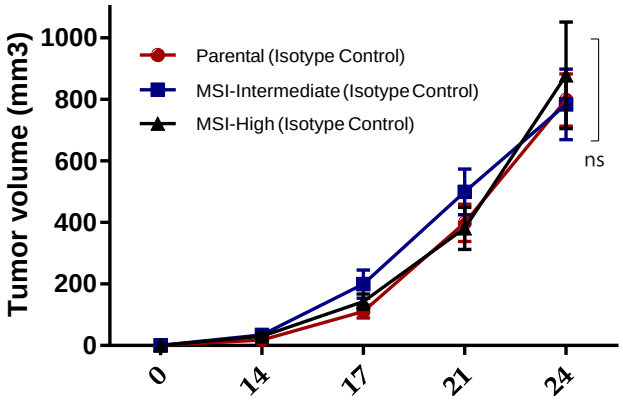

Fig. S5.

Similar baseline tumor kinetics in parental and MSI-Intermediate and MSI-High B16F10 cell line derivatives. In vivo tumor growth kinetics in isotype control antibody treated parental, MSI-Intermediate, and MSI-High tumor-bearing mice over a 24-day period (*p*=ns at day 24; Means ± SEM analyzed at end therapy by one-way ANOVA with Tukey's correction for multiple comparisons) (*n*=8-12 mice per treatment group).

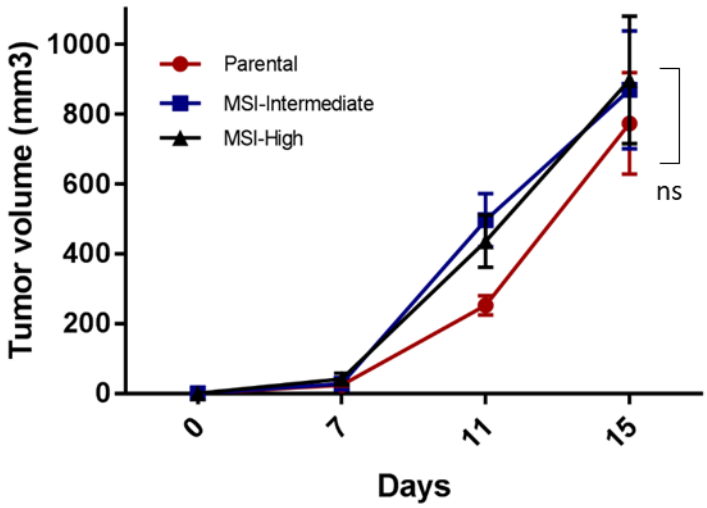

Fig. S6.

Efficient and similar baseline tumor kinetics in parental, MSI-Intermediate, and MSI-High CT26 cell line derivatives in athymic nude mice. In vivo tumor growth kinetics in untreated parental, MSI-Intermediate, and MSI-High tumor-bearing mice over a 24-day period. (*p*=ns at day 15; Means ± SEM analyzed at end therapy by one-way ANOVA with Tukey's correction for multiple comparisons) (*n*=5 mice per treatment group).

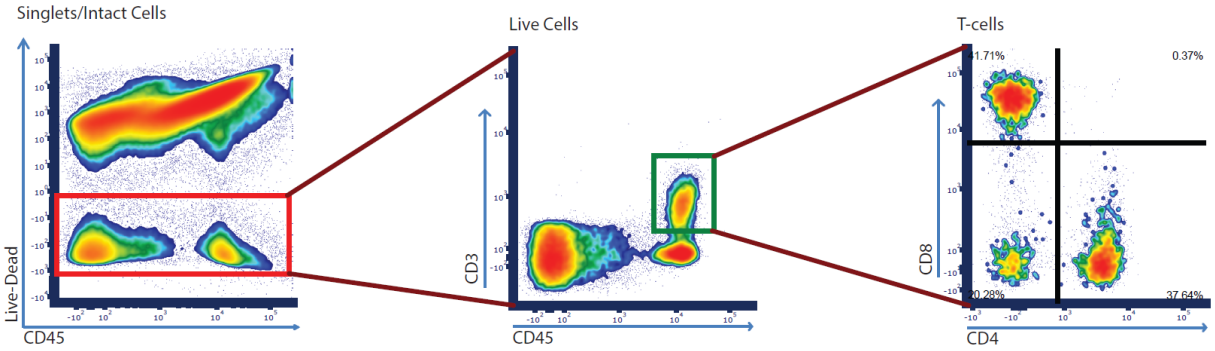

Fig. S7.

Representative flow cytometric gating strategy for mouse tumor infiltrating lymphocytes (TILs). Cells are pre-gated on singlets/intact cells. Zombie aqua live-dead stain used to gate live cells, T-cells gated on $CD3^{+}CD45^{+}$ population, $CD8^{+}$ and $CD4^{+}$ T-cell populations (*n*= 6-8 pooled tumor samples per experimental arm).

A.

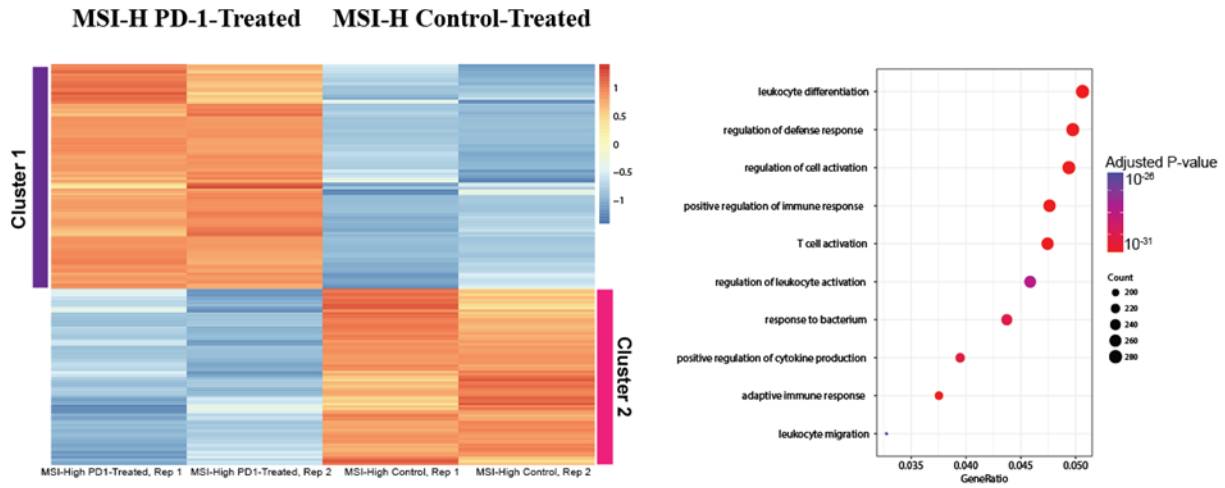

B.

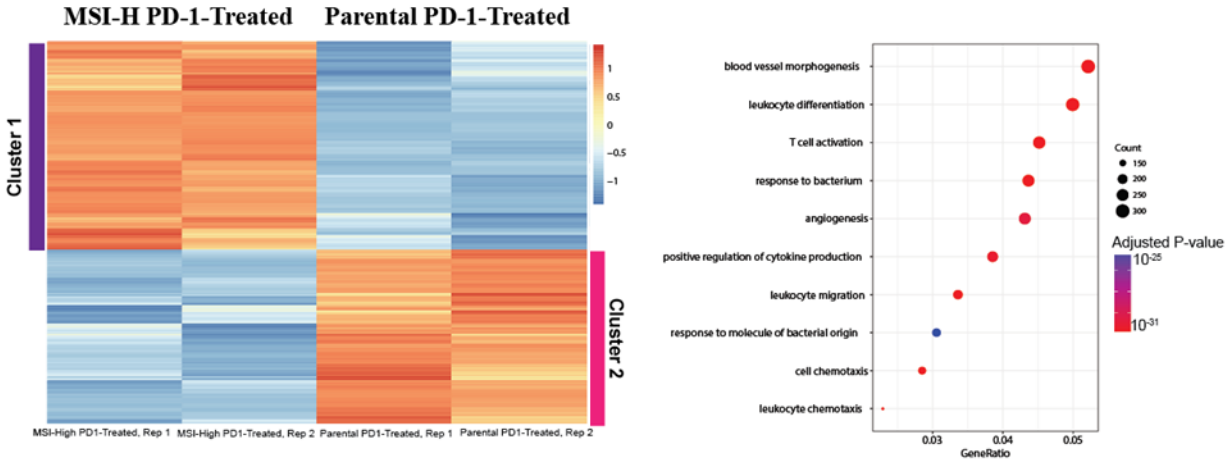

Fig. S8.

Transcriptome analysis of B16F10 mouse MSI-H tumors. Unsupervised hierarchal clustering of differentially expressed genes between (**A**) MSI-high anti-PD-1-treated vs. MSI-high isotype control-treated tumors and (**B**) MSI-high anti-PD-1-treated vs. parental anti-PD-1 treated tumors, demonstrating enrichment of immune related pathways in concordance with a more activated immune microenvironment.

A.

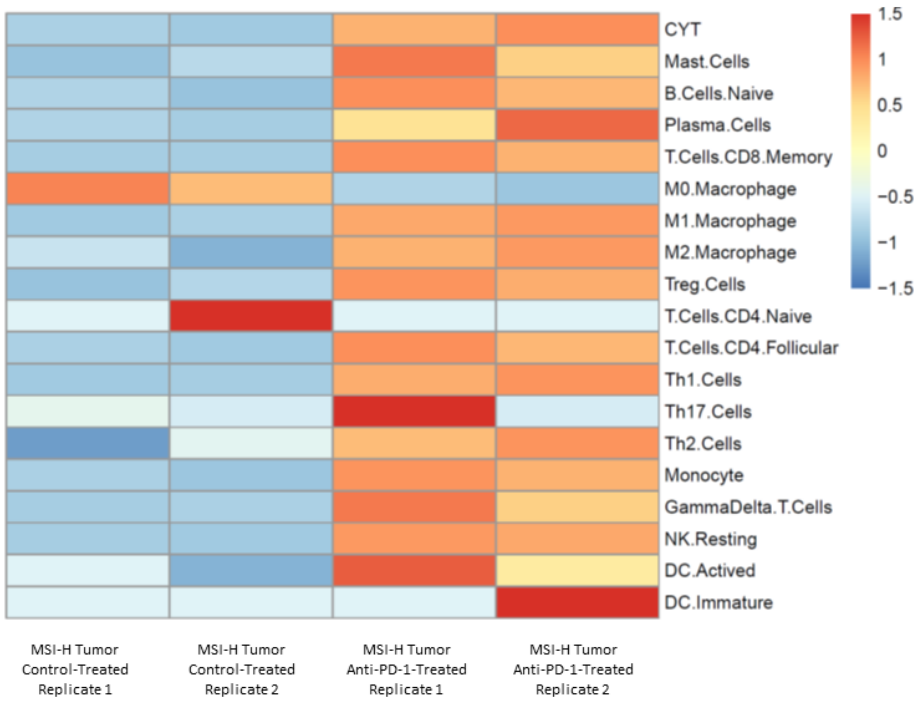

Fig. S9.

Transcriptomic immune subpopulation analysis of B16F10 mouse MSI-H tumors. Hierarchical clustering of CIBERSORT and CYT cell populations between MSI-H-anti-PD1-treated and MSI-H-isotype control-treated mouse B16F10 tumors, revealing globally higher expression levels of immune infiltration in MSI-H-anti-PD1-treated tumors as compared to isotype control-treated tumors.

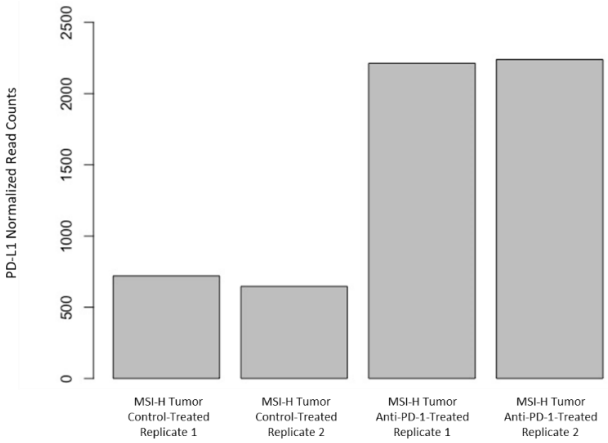

Fig. S10.

PD-L1 expression levels in B16F10 mouse MSI-H tumors. RNA-seq based DESeq2-normalized read counts of PD-L1 gene expression in MSI-H isotype control tumors vs. MSI-H anti-PD-1-treated tumors.

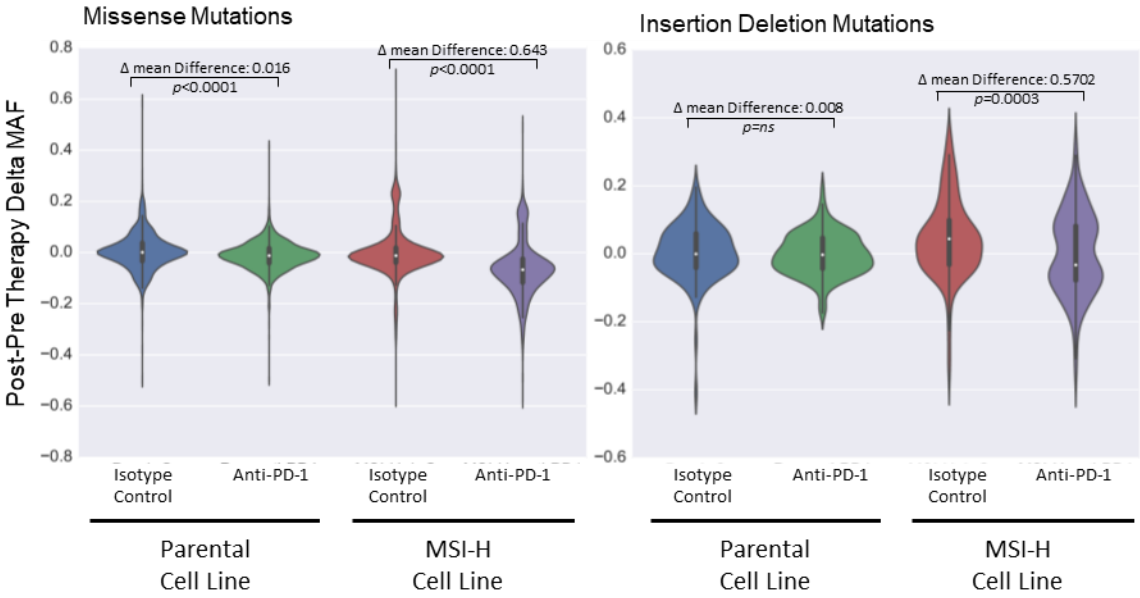

Fig. S11.

Editing of missense and indel mutations in MSI-H anti-PD-1-treated tumors. (A) Violin plots depicting the purity-corrected frequency distribution of change (Δ) in mutational allelic frequency (maf) between the post-and pre-therapy samples of missense (non-synonymous SNVs) and indel mutations in B16F10 parental and MSI-H tumors. *p* values for the comparisons in the delta means between indicated groups as shown (isotype control vs. anti-PD-1 treatment for each respective line), one-way ANOVA with Holm Sidak correction for the two comparisons on each respective panel.

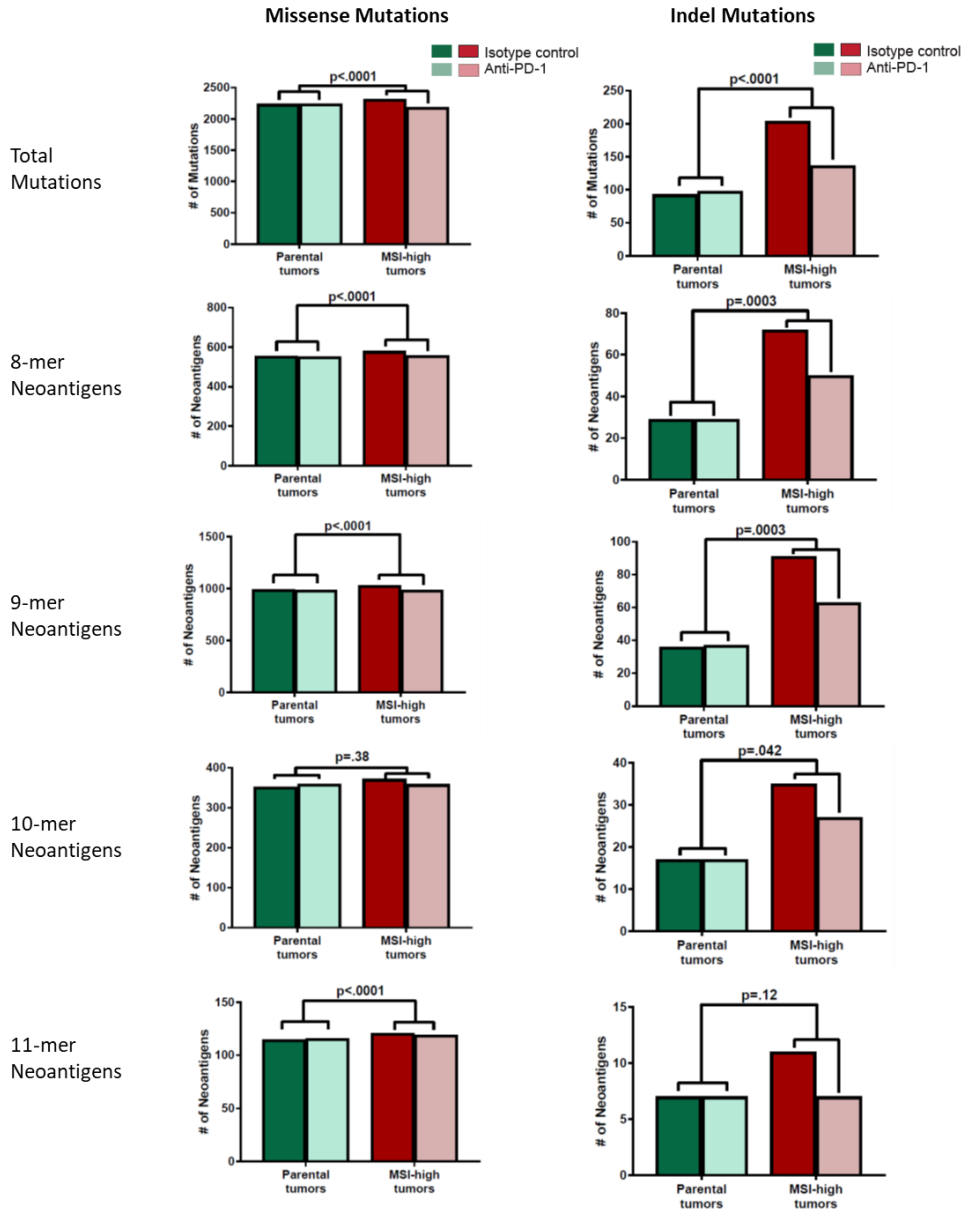

Fig. S12.

Immunoediting of Predicted Neoantigen in MSI-H tumors. Reduction in predicted 8-mer, 9-mer, 10-mer, and 11-mer neoantigen loads (missense and indel-derived neoantigens) in post-therapy isotype control/anti-PD-1-treated parental and MSI-H tumors (*p* values as indicated, Fisher's exact test for proportions of lost/gained of mutations after PD-1 blockade between indicated groups).

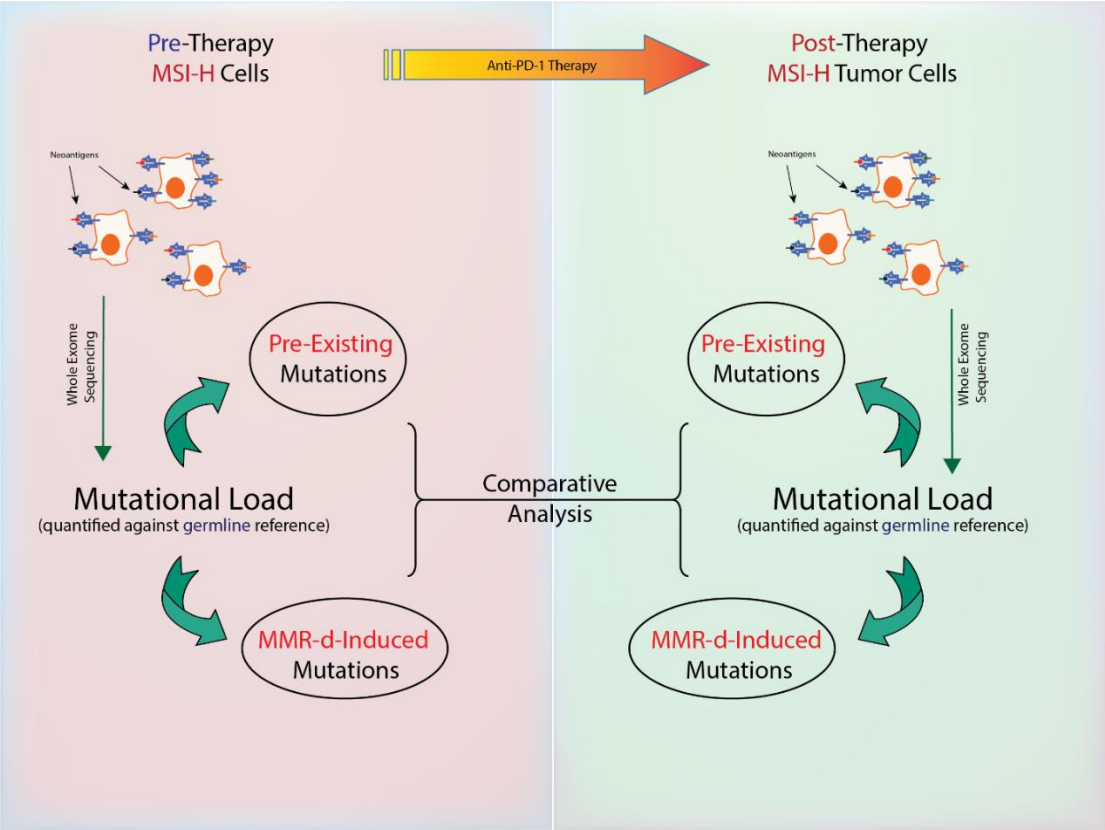

Fig. S13.

Mutational evolution following anti-PD-1-therapy in MSI-H tumor cells. Illustrative schematic depicting mutational sub-compartmental comparative analyses following whole exome sequencing of MSI-H cells pre- and post-anti-PD-1 therapy.

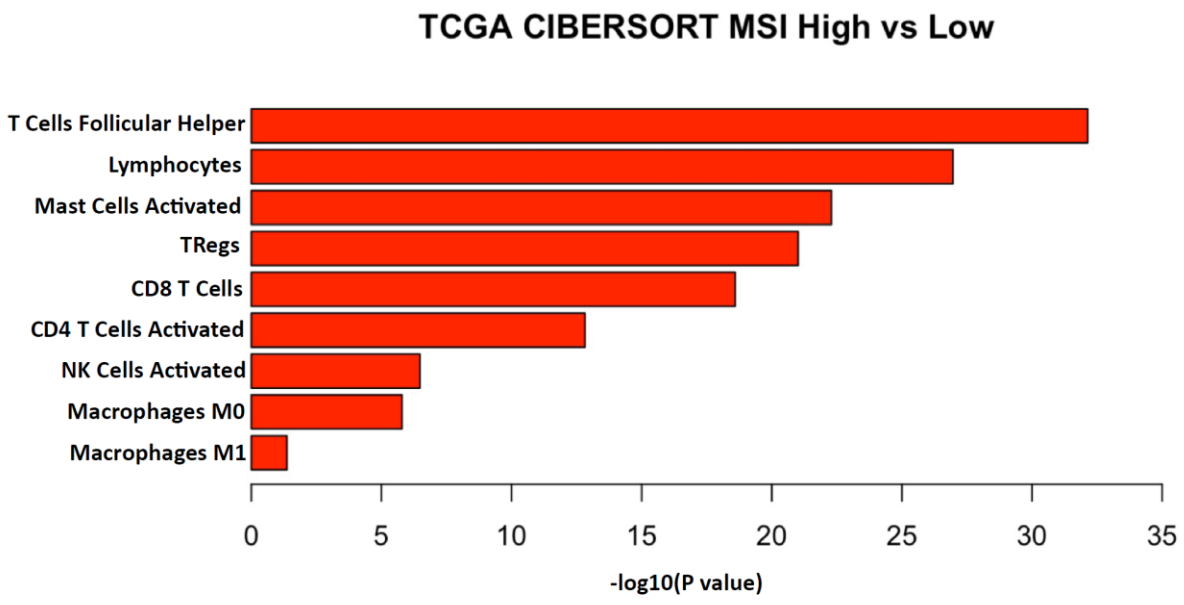

Fig. S14.

Transcriptomic immune subpopulation analysis of TCGA MSI-H and MSI-L samples. CIBERSORT cell populations with significantly higher (FDR $p < 0.05$) levels of infiltrate in TCGA MSI-high samples compared to MSI-low samples. *p* values are calculated from one-sided Mann-Whitney test and FDR-corrected using the Benjamini-Hochberg method.

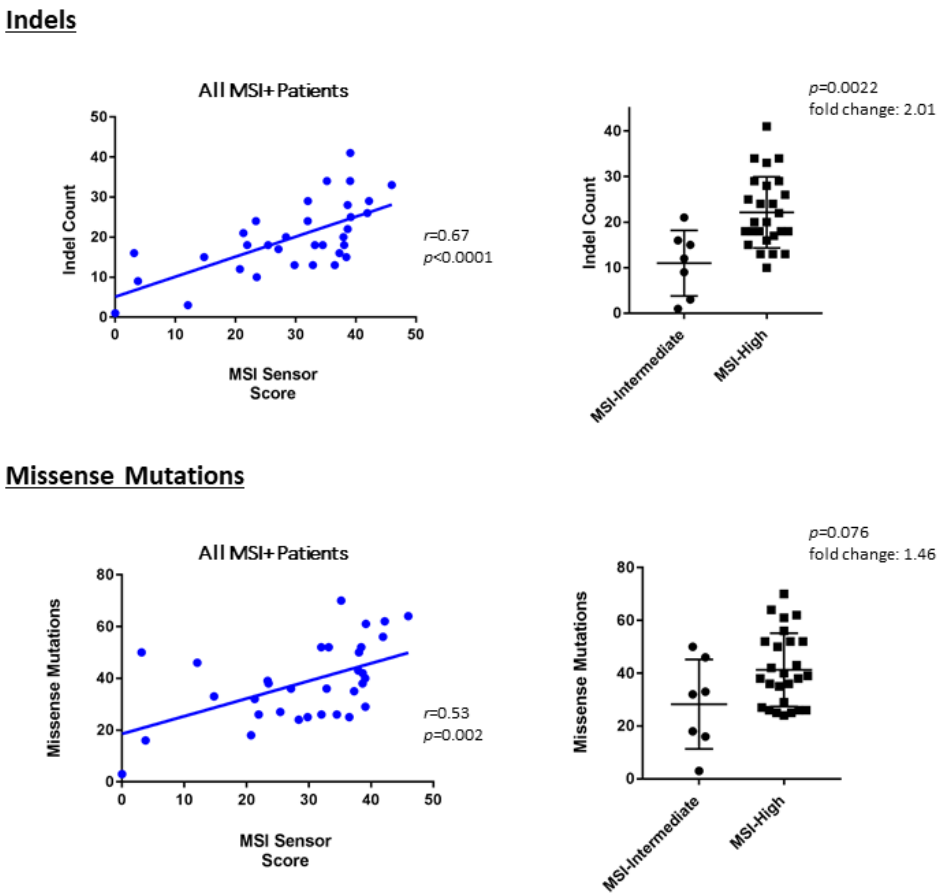

Fig. S15.

Indel and missense mutations in MSI-intermediate and MSI-high patient cohorts. Correlations between MSI sensor scores and indel/missense mutations in MMR-d human patients treated with checkpoint blockade. Indel and missense counts stratified by the MSI-intermediate and MSI-high subgroups of MMR-d patients treated with checkpoint blockade demonstrating a greater enrichment of indel mutations over missense mutations in the MSI-high subgroup compared to the MSI-intermediate subgroup (*p* values as indicated, unpaired *t*-test).

Table S1 (separate supplemental file)
Pan-Cancer CYT Scores from TCGA data.

Table S2 (separate supplemental file)
Pan-Cancer MSIsensor Scores from TCGA data.

Subject ID	WHO/RECIST Response Rate	MSI Status	MSI Senor Score
1-011	PR	MSI+	0.71
1-004	PD	MSI+	12.25
1-001	SD	MSI+	21.39
1-006	PD	MSI+	4.41
1-009	SD	MSI+	15.48
1-019	PR	MSI+	14.77
1-008	PR	MSI+	17.23
1-015	CR	MSI+	19.19
1-016	CR	MSI+	33.52

Table S3

Updated Clinical Data in JHU Cohort (WHO/RECIST Response Rate).

	MSI-Intermediate *n* (%)	**MSI-High *n* (%)**
Gender		
Female	4 (57)	9 (35)
Male	3 (43)	17 (65)
Cancer Type		
Colorectal	4 (57)	23 (88)
Esophagogastric	3 (42)	3 (12)
Drug Class		
CTLA4 targeted	1 (14)	0 (0)
PD-1/PD-L1 targeted	5 (71)	25 (96)
Combination of above	1 (14)	1 (4)
Age		
<30	0 (0)	2 (8)
31-50	2 (29)	4 (15)
51-60	2 (29)	5 (19)
61-70	2 (29)	10 (38)
>71	1 (14)	5 (19)

Table S4

Patient Clinical Demographics (MSKCC Cohort).

	Univariate Analysis		Multivariable Analysis		
	HR	**P value**	**HR**	**95% CI**	**P value**
MSI Level MSI-intermediate MSI-high	 ref 0.15	 0.01	 0.18	 0.03-0.96	 0.04
Normalized Mutation Count (TMB) > Median	0.41	0.29	0.51	0.08-3.03	0.46
Cancer Type Colorectal Esophago-gastric	 ref 4.54	 0.05	 2.15	 0.36-12.76	 0.39

Table S5
Multivariable Analysis for Overall Survival Data.

	HR	P value
MSI-high	0.06	0.014
TMBtop20%	0.17	0.155

	HR	P value
MSI-high	0.138	0.014
TMBtop40%	0.96	0.434

	HR	P value
MSI-high	0.13	0.012
TMBtop50%	0.40	0.963

	HR	P value
MSI-high	0.135	0.014
TMBtop60%	0.54	0.434

	HR	P value
MSI-high	0.15	0.016
TMBtop80%	0.56	0.466

Table S6

Multivariable analyses utilizing multiple TMB thresholds.

References and Notes

1. N. A. Rizvi, M. D. Hellmann, A. Snyder, P. Kvistborg, V. Makarov, J. J. Havel, W. Lee, J. Yuan, P. Wong, T. S. Ho, M. L. Miller, N. Rekhtman, A. L. Moreira, F. Ibrahim, C. Bruggeman, B. Gasmi, R. Zappasodi, Y. Maeda, C. Sander, E. B. Garon, T. Merghoub, J. D. Wolchok, T. N. Schumacher, T. A. Chan, Mutational landscape determines sensitivity to PD-1 blockade in non-small cell lung cancer. *Science* **348**, 124–128 (2015). doi:10.1126/science.aaa1348 Medline

2. A. Snyder, V. Makarov, T. Merghoub, J. Yuan, J. M. Zaretsky, A. Desrichard, L. A. Walsh, M. A. Postow, P. Wong, T. S. Ho, T. J. Hollmann, C. Bruggeman, K. Kannan, Y. Li, C. Elipenahli, C. Liu, C. T. Harbison, L. Wang, A. Ribas, J. D. Wolchok, T. A. Chan, Genetic basis for clinical response to CTLA-4 blockade in melanoma. *N. Engl. J. Med.* **371**, 2189–2199 (2014). doi:10.1056/NEJMoa1406498 Medline

3. E. M. Van Allen, D. Miao, B. Schilling, S. A. Shukla, C. Blank, L. Zimmer, A. Sucker, U. Hillen, M. H. G. Foppen, S. M. Goldinger, J. Utikal, J. C. Hassel, B. Weide, K. C. Kaehler, C. Loquai, P. Mohr, R. Gutzmer, R. Dummer, S. Gabriel, C. J. Wu, D. Schadendorf, L. A. Garraway, Genomic correlates of response to CTLA-4 blockade in metastatic melanoma. *Science* **350**, 207–211 (2015). doi:10.1126/science.aad0095 Medline

4. F. Supek, B. Lehner, Differential DNA mismatch repair underlies mutation rate variation across the human genome. *Nature* **521**, 81–84 (2015). doi:10.1038/nature14173 Medline

5. D. T. Le, J. N. Durham, K. N. Smith, H. Wang, B. R. Bartlett, L. K. Aulakh, S. Lu, H. Kemberling, C. Wilt, B. S. Luber, F. Wong, N. S. Azad, A. A. Rucki, D. Laheru, R. Donehower, A. Zaheer, G. A. Fisher, T. S. Crocenzi, J. J. Lee, T. F. Greten, A. G. Duffy, K. K. Ciombor, A. D. Eyring, B. H. Lam, A. Joe, S. P. Kang, M. Holdhoff, L. Danilova, L. Cope, C. Meyer, S. Zhou, R. M. Goldberg, D. K. Armstrong, K. M. Bever, A. N. Fader, J. Taube, F. Housseau, D. Spetzler, N. Xiao, D. M. Pardoll, N. Papadopoulos, K. W. Kinzler, J. R. Eshleman, B. Vogelstein, R. A. Anders, L. A. Diaz Jr., Mismatch repair deficiency predicts response of solid tumors to PD-1 blockade. *Science* **357**, 409–413 (2017). doi:10.1126/science.aan6733 Medline

6. D. T. Le, J. N. Uram, H. Wang, B. R. Bartlett, H. Kemberling, A. D. Eyring, A. D. Skora, B. S. Luber, N. S. Azad, D. Laheru, B. Biedrzycki, R. C. Donehower, A. Zaheer, G. A. Fisher, T. S. Crocenzi, J. J. Lee, S. M. Duffy, R. M. Goldberg, A. de la Chapelle, M. Koshiji, F. Bhaijee, T. Huebner, R. H. Hruban, L. D. Wood, N. Cuka, D. M. Pardoll, N. Papadopoulos, K. W. Kinzler, S. Zhou, T. C. Cornish, J. M. Taube, R. A. Anders, J. R. Eshleman, B. Vogelstein, L. A. Diaz Jr., PD-1 Blockade in Tumors with Mismatch-Repair Deficiency. *N. Engl. J. Med.* **372**, 2509–2520 (2015). doi:10.1056/NEJMoa1500596 Medline

7. U.S. Food and Drug Administration, FDA approves first cancer treatment for any solid tumor with a specific genetic feature (FDA News Release, 23 May 2017).

8. G. Germano, S. Lamba, G. Rospo, L. Barault, A. Magrì, F. Maione, M. Russo, G. Crisafulli, A. Bartolini, G. Lerda, G. Siravegna, B. Mussolin, R. Frapolli, M. Montone, F. Morano, F. de Braud, N. Amirouchene-Angelozzi, S. Marsoni, M. D'Incalci, A. Orlandi, E. Giraudo, A. Sartore-Bianchi, S. Siena, F. Pietrantonio, F. Di Nicolantonio, A. Bardelli,

Inactivation of DNA repair triggers neoantigen generation and impairs tumour growth. *Nature* **552**, 116–120 (2017). doi:10.1038/nature24673 Medline

9. J. Drost, R. van Boxtel, F. Blokzijl, T. Mizutani, N. Sasaki, V. Sasselli, J. de Ligt, S. Behjati, J. E. Grolleman, T. van Wezel, S. Nik-Zainal, R. P. Kuiper, E. Cuppen, H. Clevers, Use of CRISPR-modified human stem cell organoids to study the origin of mutational signatures in cancer. *Science* **358**, 234–238 (2017). doi:10.1126/science.aao3130 Medline

10. B. Niu, K. Ye, Q. Zhang, C. Lu, M. Xie, M. D. McLellan, M. C. Wendl, L. Ding, MSIsensor: Microsatellite instability detection using paired tumor-normal sequence data. *Bioinformatics* **30**, 1015–1016 (2014). doi:10.1093/bioinformatics/btt755 Medline

11. S. Turajlic, K. Litchfield, H. Xu, R. Rosenthal, N. McGranahan, J. L. Reading, Y. N. S. Wong, A. Rowan, N. Kanu, M. Al Bakir, T. Chambers, R. Salgado, P. Savas, S. Loi, N. J. Birkbak, L. Sansregret, M. Gore, J. Larkin, S. A. Quezada, C. Swanton, Insertion-and-deletion-derived tumour-specific neoantigens and the immunogenic phenotype: A pan-cancer analysis. *Lancet Oncol.* **18**, 1009–1021 (2017). doi:10.1016/S1470-2045(17)30516-8 Medline

12. M. R. Kohonen-Corish, J. J. Daniel, C. Chan, B. P. C. Lin, S. Y. Kwun, O. F. Dent, V. S. Dhillon, R. J. A. Trent, P. H. Chapuis, E. L. Bokey, Low microsatellite instability is associated with poor prognosis in stage C colon cancer. *J. Clin. Oncol.* **23**, 2318–2324 (2005). doi:10.1200/JCO.2005.00.109 Medline

13. S. Ogino, A. Goel, Molecular classification and correlates in colorectal cancer. *J. Mol. Diagn.* **10**, 13–27 (2008). doi:10.2353/jmoldx.2008.070082 Medline

14. R. J. Hause, C. C. Pritchard, J. Shendure, S. J. Salipante, Classification and characterization of microsatellite instability across 18 cancer types. *Nat. Med.* **22**, 1342–1350 (2016). doi:10.1038/nm.4191 Medline

15. T. M. Kim, P. W. Laird, P. J. Park, The landscape of microsatellite instability in colorectal and endometrial cancer genomes. *Cell* **155**, 858–868 (2013). doi:10.1016/j.cell.2013.10.015 Medline

16. S. J. Salipante, S. M. Scroggins, H. L. Hampel, E. H. Turner, C. C. Pritchard, Microsatellite instability detection by next generation sequencing. *Clin. Chem.* **60**, 1192–1199 (2014). doi:10.1373/clinchem.2014.223677 Medline

17. Y. Y. Janjigian, F. Sanchez-Vega, P. Jonsson, W. K. Chatila, J. F. Hechtman, G. Y. Ku, J. C. Riches, Y. Tuvy, R. Kundra, N. Bouvier, E. Vakiani, J. Gao, Z. J. Heins, B. E. Gross, D. P. Kelsen, L. Zhang, V. E. Strong, M. Schattner, H. Gerdes, D. G. Coit, M. Bains, Z. K. Stadler, V. W. Rusch, D. R. Jones, D. Molena, J. Shia, M. E. Robson, M. Capanu, S. Middha, A. Zehir, D. M. Hyman, M. Scaltriti, M. Ladanyi, N. Rosen, D. H. Ilson, M. F. Berger, L. Tang, B. S. Taylor, D. B. Solit, N. Schultz, Genetic Predictors of Response to Systemic Therapy in Esophagogastric Cancer. *Cancer Discov.* **8**, 49–58 (2018). doi:10.1158/2159-8290.CD-17-0787 Medline

18. R. Yaeger, W. K. Chatila, M. D. Lipsyc, J. F. Hechtman, A. Cercek, F. Sanchez-Vega, G. Jayakumaran, S. Middha, A. Zehir, M. T. A. Donoghue, D. You, A. Viale, N. Kemeny, N. H. Segal, Z. K. Stadler, A. M. Varghese, R. Kundra, J. Gao, A. Syed, D. M. Hyman, E. Vakiani, N. Rosen, B. S. Taylor, M. Ladanyi, M. F. Berger, D. B. Solit, J. Shia, L.

Saltz, N. Schultz, Clinical Sequencing Defines the Genomic Landscape of Metastatic Colorectal Cancer. *Cancer Cell* **33**, 125–136.e3 (2018). doi:10.1016/j.ccell.2017.12.004 Medline

19. A. Zehir, R. Benayed, R. H. Shah, A. Syed, S. Middha, H. R. Kim, P. Srinivasan, J. Gao, D. Chakravarty, S. M. Devlin, M. D. Hellmann, D. A. Barron, A. M. Schram, M. Hameed, S. Dogan, D. S. Ross, J. F. Hechtman, D. F. DeLair, J. Yao, D. L. Mandelker, D. T. Cheng, R. Chandramohan, A. S. Mohanty, R. N. Ptashkin, G. Jayakumaran, M. Prasad, M. H. Syed, A. B. Rema, Z. Y. Liu, K. Nafa, L. Borsu, J. Sadowska, J. Casanova, R. Bacares, I. J. Kiecka, A. Razumova, J. B. Son, L. Stewart, T. Baldi, K. A. Mullaney, H. Al-Ahmadie, E. Vakiani, A. A. Abeshouse, A. V. Penson, P. Jonsson, N. Camacho, M. T. Chang, H. H. Won, B. E. Gross, R. Kundra, Z. J. Heins, H.-W. Chen, S. Phillips, H. Zhang, J. Wang, A. Ochoa, J. Wills, M. Eubank, S. B. Thomas, S. M. Gardos, D. N. Reales, J. Galle, R. Durany, R. Cambria, W. Abida, A. Cercek, D. R. Feldman, M. M. Gounder, A. A. Hakimi, J. J. Harding, G. Iyer, Y. Y. Janjigian, E. J. Jordan, C. M. Kelly, M. A. Lowery, L. G. T. Morris, A. M. Omuro, N. Raj, P. Razavi, A. N. Shoushtari, N. Shukla, T. E. Soumerai, A. M. Varghese, R. Yaeger, J. Coleman, B. Bochner, G. J. Riely, L. B. Saltz, H. I. Scher, P. J. Sabbatini, M. E. Robson, D. S. Klimstra, B. S. Taylor, J. Baselga, N. Schultz, D. M. Hyman, M. E. Arcila, D. B. Solit, M. Ladanyi, M. F. Berger, Mutational landscape of metastatic cancer revealed from prospective clinical sequencing of 10,000 patients. *Nat. Med.* **23**, 703–713 (2017). doi:10.1038/nm.4333 Medline

20. S. Middha, L. Zhang, K. Nafa, G. Jayakumaran, D. Wong, H. R. Kim, J. Sadowska, M. F. Berger, D. F. Delair, J. Shia, Z. Stadler, D. S. Klimstra, M. Ladanyi, A. Zehir, J. F. Hechtman, Reliable Pan-Cancer Microsatellite Instability Assessment by Using Targeted Next-Generation Sequencing Data. *JCO Precision Oncology* **2017**, 1–17 (2017). doi:10.1200/PO.17.00084 Medline

21. F. A. Ran, P. D. Hsu, J. Wright, V. Agarwala, D. A. Scott, F. Zhang, Genome engineering using the CRISPR-Cas9 system. *Nat. Protoc.* **8**, 2281–2308 (2013). doi:10.1038/nprot.2013.143 Medline

22. N. Riaz, J. J. Havel, V. Makarov, A. Desrichard, W. J. Urba, J. S. Sims, F. S. Hodi, S. Martín-Algarra, R. Mandal, W. H. Sharfman, S. Bhatia, W.-J. Hwu, T. F. Gajewski, C. L. Slingluff Jr., D. Chowell, S. M. Kendall, H. Chang, R. Shah, F. Kuo, L. G. T. Morris, J.-W. Sidhom, J. P. Schneck, C. E. Horak, N. Weinhold, T. A. Chan, Tumor and Microenvironment Evolution during Immunotherapy with Nivolumab. *Cell* **171**, 934–949.e16 (2017). doi:10.1016/j.cell.2017.09.028 Medline

23. N. Riaz, J. J. Havel, S. M. Kendall, V. Makarov, L. A. Walsh, A. Desrichard, N. Weinhold, T. A. Chan, Recurrent SERPINB3 and SERPINB4 mutations in patients who respond to anti-CTLA4 immunotherapy. *Nat. Genet.* **48**, 1327–1329 (2016). doi:10.1038/ng.3677 Medline

24. K. Yoshihara, M. Shahmoradgoli, E. Martínez, R. Vegesna, H. Kim, W. Torres-Garcia, V. Treviño, H. Shen, P. W. Laird, D. A. Levine, S. L. Carter, G. Getz, K. Stemke-Hale, G. B. Mills, R. G. W. Verhaak, Inferring tumour purity and stromal and immune cell admixture from expression data. *Nat. Commun.* **4**, 2612 (2013). doi:10.1038/ncomms3612 Medline

25. M. S. Rooney, S. A. Shukla, C. J. Wu, G. Getz, N. Hacohen, Molecular and genetic properties of tumors associated with local immune cytolytic activity. *Cell* **160**, 48–61 (2015). doi:10.1016/j.cell.2014.12.033 Medline

26. B. Niu, K. Ye, Q. Zhang, C. Lu, M. Xie, M. D. McLellan, M. C. Wendl, L. Ding, MSIsensor: Microsatellite instability detection using paired tumor-normal sequence data. *Bioinformatics* **30**, 1015–1016 (2014). doi:10.1093/bioinformatics/btt755 Medline

27. R. J. Hause, C. C. Pritchard, J. Shendure, S. J. Salipante, Classification and characterization of microsatellite instability across 18 cancer types. *Nat. Med.* **22**, 1342–1350 (2016). doi:10.1038/nm.4191 Medline

28. T. M. Kim, P. W. Laird, P. J. Park, The landscape of microsatellite instability in colorectal and endometrial cancer genomes. *Cell* **155**, 858–868 (2013). doi:10.1016/j.cell.2013.10.015 Medline

29. D. T. Le, J. N. Uram, H. Wang, B. R. Bartlett, H. Kemberling, A. D. Eyring, A. D. Skora, B. S. Luber, N. S. Azad, D. Laheru, B. Biedrzycki, R. C. Donehower, A. Zaheer, G. A. Fisher, T. S. Crocenzi, J. J. Lee, S. M. Duffy, R. M. Goldberg, A. de la Chapelle, M. Koshiji, F. Bhaijee, T. Huebner, R. H. Hruban, L. D. Wood, N. Cuka, D. M. Pardoll, N. Papadopoulos, K. W. Kinzler, S. Zhou, T. C. Cornish, J. M. Taube, R. A. Anders, J. R. Eshleman, B. Vogelstein, L. A. Diaz Jr., PD-1 Blockade in Tumors with Mismatch-Repair Deficiency. *N. Engl. J. Med.* **372**, 2509–2520 (2015). doi:10.1056/NEJMoa1500596 Medline